Received: DD MM YYYY | Revised: DD MM YYYY | Accepted: DD MM YYYY

DOI: 10.1109/xxx.xx.xxxx

ORIGINAL PAPER

Lander-Aided Differential Doppler and One-Way Ranging for Lunar Rover Navigation with a Single Relay Satellite

Kaila M. Y. Coimbra | Grace Gao

[1]Department of Aeronautics and Astronautics, Stanford University

Correspondence

*Grace Gao, Department of Aeronautics and Astronautics, Stanford University
Stanford, CA, USA 94305
Email: gracegao@stanford.edu

Abstract

As lunar exploration expands, long-range lunar rovers will require positioning methods that remain available when imagery is unreliable and navigation infrastructure is sparse. This paper evaluates a minimal three-node architecture in which a rover localizes using a single lunar relay satellite, its lander, and onboard odometry. The relay is treated as a communications spacecraft rather than a navigation satellite such that the rover only measures one-way Doppler from the relay downlink. The lander provides one-way pseudorange to the rover, and we also investigate the improvement in localization performance when the lander forwards its relay Doppler observation from the satellite so that the rover can form a lander-aided differential Doppler measurement. An extended Kalman Filter is developed for each measurement configuration, with clock states matched to the links and a Schmidt-Kalman consider-state treatment for broadcast ephemeris error when raw satellite Doppler is used. The simulation includes stochastic rover, lander, and satellite clocks; time-correlated relay ephemeris errors with periodic ODTS updates; thermal measurement noise from link budgets; and mission profiles with continuous, lost, and reacquired lander line of sight. A Fisher-information observability analysis shows that single-satellite Doppler most strongly constrains directions along the satellite sky-track sweep, while lander pseudorange supplies a stable but nearly one-dimensional surface constraint. Combining the two measurement sources removes the kilometer-scale weak horizontal direction present in the satellite-only case and improves vertical observability relative to the lander-only case. In a constant-visibility ablation, the differential satellite-and-lander configuration performs best, reaching sub-10-m three-dimensional position error after 1.8 hours from an initial position error of 100 m per-axis and maintaining that accuracy over 24 hours. In scenarios with surface-link loss or reacquisition, the estimator preserves accuracy through configuration switching. Lander loss leads to odometry-like growth until ephemeris updates restore Doppler utility, while reacquiring the lander reduces the mean error by roughly 60 m. These results show that a landed asset can strengthen lunar rover navigation without requiring a dedicated satellite navigation payload.

Keywords

Lunar navigation, differential Doppler, weak observability

1 | INTRODUCTION

International space agencies and commercial companies are planning a range of lunar missions, from deploying lunar communications and navigation satellites in orbit (Giordano et al., 2023) to returning humans to the lunar surface (Watson-Morgan, 2023). In the near term, many efforts emphasize exploratory robotic missions in the lunar south polar region as precursors to sustained surface operations. These architectures frequently pair a landed element with one or more spacecraft in lunar orbit that provide communications relay and operational support for surface assets. For example, NASA's Artemis campaign pursues a Human Landing System that transfers to a lunar orbit prior to descent, and commercial providers including Blue Origin have been contracted to deliver crew and cargo landers for lunar surface operations (Watson-Morgan, 2023). This lander-and-orbit configuration motivates leveraging existing mission infrastructure for rover positioning and navigation. For early-stage rover missions, precise absolute localization is needed to support long-range traverses, science targeting, and safe operations in challenging terrain. In this work, we evaluate the localization performance of a rover using three sources of measurements: one-way Doppler shift from the downlink communication signal of a relay satellite, one-way ranging measurements from the lander that deployed the rover, and the rover's onboard odometry module.

1.1 | Related Work and Limitations

Many works have investigated vision-based lunar rover navigation, including crater-based map matching and factor graph methods (Cauligi et al., 2023; Daftry et al., 2023; Dai et al., 2025). However, long-range rovers operating across the lunar day-night cycle may experience extended periods of low illumination in addition to traverses near permanently shadowed regions, unless they explicitly avoid those areas. These constraints motivate navigation approaches that do not depend on continuous high-quality imagery. In this work, we utilize a minimal navigation infrastructure that is agnostic to the illumination or imagery quality of the region.

Several studies have investigated rover or surface user positioning with limited lunar infrastructure. Tanaka et al. (2025) propose a minimalist system consisting of a single satellite, a known reference station, and a stationary user. They rely on differential dual one-way ranging for faster positioning convergence in comparison to Doppler measurements. Their study focuses on relative positioning for a stationary user and assumes dual one-way ranging capability, which is distinct from the one-way Doppler signal considered in this work for the space segment. Furthermore, we evaluate our method on a continuously moving rover.

Jun et al. (2024) introduce joint Doppler and ranging (JDR) and demonstrate real-time estimation of position, velocity, and timing for lunar surface users using one-way range and Doppler measurements from two orbiters along with a surface reference station. Their simulation study assumed that the reference station's clock was synchronized, thereby reducing the emphasis on the network's clock noise. In contrast, the architecture considered in this work assumes only a single satellite and does not assume that the relay broadcasts a dedicated ranging code. We also explicitly study non-ideal clocks at the rover, lander, and satellite nodes.

In prior work by the authors, we evaluated the localization performance of a rover using only the Doppler shift of a communication signal from a single relay satellite and demonstrated convergence from an initial 100 m 3D position error to sub-10-m accuracy within two relay orbits (Coimbra et al., 2025). In the present work, we incorporate measurements available from the surface lander that deploys the rover, and we introduce a lander-aided differential Doppler correction. Analogous terrestrial approaches have investigated differential Doppler methods using low Earth orbit signals of opportunity and a reference station, including angle-of-arrival estimation (Thompson et al., 2021) and tight integration with an inertial navigation system (Zhao et al., 2025). We adapt this concept of utilizing differential Doppler to a single-relay lunar architecture. We also conduct an observability analysis to quantify the limited and unique geometry of the system.

1.2 | Proposed Work

This work evaluates the rover localization performance under a minimal navigation infrastructure concept. The mission scenario assumes a single relay satellite operating in an elliptical lunar frozen orbit modeled after the proposed orbit of ESA's Lunar Pathfinder. We assume the lander position is known through human-in-the-loop map matching or pre-mission localization within 5 m standard deviation per-axis.

The rover receives one-way Doppler measurements from the relay satellite downlink signal, as we assume that the satellite does not carry a dedicated navigation payload. The rover also receives one-way ranging measurements from the surface lander. The lander is equipped with a receiver that measures the Doppler shift of the relay downlink signal and broadcasts a differential Doppler correction to the rover. The correction is intended to reduce the sensitivity of the rover's Doppler measurements to ephemeris errors and satellite clock effects without requiring the rover to estimate the full satellite state or requiring the lander to solve a standalone orbit determination problem. The rover uses only these two external measurement sources, together with onboard inertial odometry, to estimate its position over time using an Extended Kalman Filter (EKF). The resulting measurement link configuration is shown in Figure 1. We evaluate performance across several mission cases that isolate the effects of the lander ranging link and of the lander broadcast Doppler corrections. We also perform Monte Carlo evaluations to quantify the performance across stochastic realizations of the measurement and process noise.

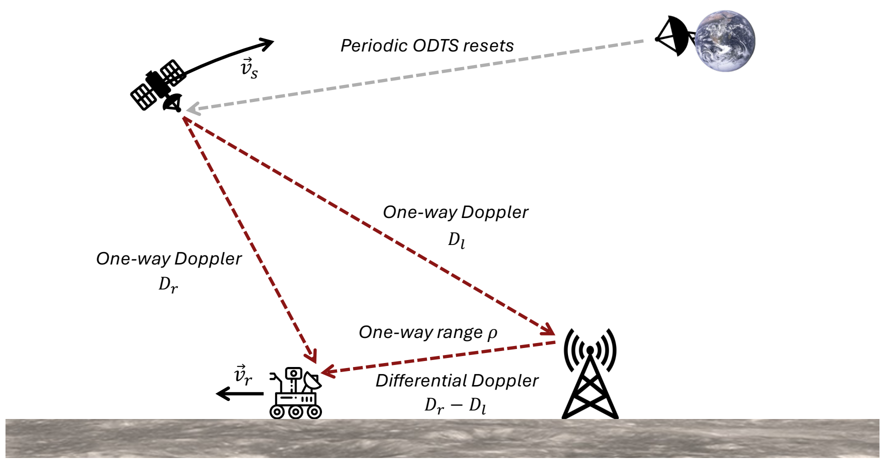

FIGURE 1 In the fully-aided scenario, the rover receives one-way Doppler measurements from the satellite and one-way range measurements from the lander, which acts as a known reference station. When the satellite is visible, the lander also receives the satellite downlink Doppler and broadcasts a differential Doppler correction to the rover. In simulation, we model periodic ODTS updates from Earth that reset the ephemeris errors, shown in gray. We include only the resulting reset effects, since modeling Earth-Moon link operations is outside the scope of this work.

1.3 | Description of New and Innovative Aspects

The novel contributions presented in this work are as follows. This work is adapted from Coimbra and Gao (2026a), originally submitted to the Institute of Navigation GNSS+ 2026 conference.

- **Lander-aided differential Doppler using minimal infrastructure:** We evaluate the localization performance of a lander-aided differential Doppler framework that fuses corrected one-way relay Doppler measurements, one-way lander-to-rover pseudorange, and rover odometry in a three-node architecture that does not assume a dedicated navigation payload onboard the relay satellite.
- **Analysis across measurement configurations and geometries:** We conduct an ablation study that isolates the value of lander ranging and the lander's broadcast Doppler corrections, and perform an observability analysis that reveals directionality limitations in single-satellite Doppler-based navigation.
- **Mission-driven evaluations with varying lander line of sight:** We evaluate rover localization across mission scenarios with different rover-lander LOS conditions, including continuous lander visibility, traversal beyond the lander radio horizon, and a lost-rover scenario in which lander LOS is later reacquired. These cases capture practical operating regimes for long-range lunar rover traverses and quantify how localization performance changes as lander measurements become available or unavailable.

1.4 | Paper Organization

The remainder of the manuscript is organized as follows. Section 2 describes the simulated asset dynamics and measurement models. The filtering framework for each measurement configuration, along with the observability analysis, is presented in Section 3. Section 4 then defines the simulation parameters used to construct the mission scenarios. The main results are reported in Section 5, including observability trends and rover localization performance across the considered scenarios. Finally, Section 6 summarizes the main findings and discusses future work.

2 | MODELING

This section presents the ground-truth dynamics and measurement models used in simulation. We briefly review the components adopted from Coimbra and Gao (2026b), including the rover and satellite motion models, clock dynamics, and satellite ephemeris error model. We then describe the link-budget assumptions used to represent realistic communication links between the assets.

Finally, we mathematically define the simulated measurements, including the satellite Doppler shift, lander-rover pseudorange, and differential Doppler correction.

2.1 | Dynamics, Clock, and Ephemeris Error Modeling

We adopt the lunar rover-satellite modeling framework from Coimbra and Gao (2026b) and summarize only the assumptions most relevant to this study. Rover motion is represented kinematically on a spherical lunar surface and is converted from a local East-North-Up (ENU) frame to a Moon-fixed frame for coherence with the satellite and lander frames. When simulating a circular trajectory around the lander, the rover follows an exact small circle on the sphere about the lander location, generated by rotating the initial rover position about the lander radial vector from the Moon's center. Rover heading is assumed known through the use of onboard attitude sensing, such as star trackers. The satellite trajectory is propagated independently in a lunar-centered inertial frame using high-fidelity lunar-orbit dynamics (100×100 spherical harmonic lunar gravitational field) and is then transformed into the same Moon-fixed frame used to represent the rover state.

Each asset's onboard clock is modeled as an independent two-state stochastic process containing clock bias and clock drift. The clock process noise is parameterized by standard oscillator noise coefficients, allowing the relative clock drift between assets to evolve over time rather than being treated as a constant unknown. Clock process noise parameters are selected based on the oscillator grade for the rover, lander, and satellite and specified in Section 4. In addition to these stochastic clock terms, we include deterministic relativistic clock-rate offsets caused by gravitational potential differences and velocity-dependent time dilation. These corrections relate each asset's proper time to lunar coordinate time (TCL) (International Astronomical Union, 2024). Details of the treatment of relativistic effects can be found in Coimbra and Gao (2026b). For ground-truth modeling, an iterative light-time solution is also applied so that the satellite state used in the link geometry corresponds to the signal transmission time rather than the rover reception time.

The rover relies on a broadcast satellite ephemeris subject to orbit determination errors. The ephemeris error is represented in Cartesian position and velocity, with the underlying acceleration error evolving as a time-correlated Singer process (Singer, 1970). Without correction, the expected ephemeris error growth is unbounded, which is not representative of plausible operations. We therefore assume that the relay periodically receives orbit determination and time synchronization (ODTS) updates, as assumed by some lunar relay specifications (Surrey Satellite Technology Ltd, 2022). Thus, the ephemeris error process is reset at prescribed update times to a small residual uncertainty rather than being driven exactly to zero. This preserves the time-correlated structure of the broadcast error while reflecting improved satellite orbit knowledge after each update. We assume the rover and lander are aware of the ODTS update times.

2.2 | Link Budget

The signal quality of each link is quantified through the carrier-to-noise density ratio C/N_0, which is a function of the received power, the receiver's gain-to-noise-temperature, and the Boltzmann constant $k_B = -228.6$ dBW/K/Hz (Delépaut et al., 2020). The received power can be broken down into the maximum effective isotropic radiated power $EIRP_0$, the parabolic antenna rolloff in terms of the off-boresight angle measured from the satellite nadir θ_t and the boresight-to-half-power angle θ_{HP}, and the free space path loss in terms of the true range between both assets r, the signal frequency f, and speed of light c. The gain-to-noise-temperature considers the receiver's gain G_r and the equivalent noise temperature T_{eq}. The definition of the carrier-to-noise density ratio C/N_0, in dB-Hz and Hz, is expanded below (Misra & Enge, 2012).

$$\left(\frac{C}{N_0}\right)_{\text{dB-Hz}} = EIRP_0 - 3\left(\frac{\theta_t}{\theta_{HP}}\right)^2 - 20\log_{10}\left(\frac{4\pi r f}{c}\right) + G_r - 10\log_{10} T_{eq} - k_B \tag{1}$$

$$\left(\frac{C}{N_0}\right)_{\text{Hz}} = 10^{(C/N_0)_{\text{dB-Hz}}/10} \tag{2}$$

Each signal link uses a frequency f, maximum EIRP, and receiver gain G_r that align with the expected parameters for each asset, resulting in varying signal quality for each link. The values are summarized in Section 4.

In this work, a smooth sphere approximation is used to isolate the performance due to radiometric measurements only without having to account for signal obstructions from the terrain. Under this smooth-sphere model, we model surface-link availability using a line-of-sight cutoff. The maximum surface separation s_{max} between the rover and lander is geometrically derived in terms of the Moon's radius R_M, and the antenna heights of the rover h_r and lander h_l.

$$s_{max} \simeq \sqrt{2R_M h_r} + \sqrt{2R_M h_l} \tag{3}$$

In simulation, the lander-rover link is disconnected when the distance between the lander and rover exceeds the maximum surface separation. High-fidelity near-horizon propagation effects, such as diffraction or multipath, are outside the scope of this study.

2.3 | Radiometric Measurement Modeling

The rover uses odometry and satellite radio measurements for localization. As defined in Coimbra and Gao (2026b), odometry is modeled as a noisy incremental displacement measurement, with uncertainty proportional to the distance traveled over each propagation interval. This approximation aggregates wheel slip, inertial sensing error, and other local rover motion errors into a simplified odometry noise model.

2.3.1 | Observed Doppler Shift

The Doppler observable from the satellite's communication signal is modeled as a pseudorange rate measurement $\dot{\rho}$. The observed pseudorange rate $\tilde{\dot{\rho}}$ includes contributions from the relative clock drift and the measurement noise $\varepsilon_{\dot{\rho}}$ with variance $\sigma^2_{\dot{\rho}}$. The formulation for the pseudorange rate between the satellite (s) and the rover (r) is shown below.

$$\tilde{\dot{\rho}}_r = (\mathbf{v}_s^* - \mathbf{v}_r) \cdot \frac{\mathbf{r}_s^* - \mathbf{r}_r}{\|\mathbf{r}_s^* - \mathbf{r}_r\|} + c\left(\dot{\delta t}_r - \dot{\delta t}_s\right) + \varepsilon_{\dot{\rho},r} \quad , \quad \varepsilon_{\dot{\rho},r} \sim \mathcal{N}\left(0, \sigma^2_{\dot{\rho},r}\right) \tag{4}$$

The variables $(\mathbf{r}_s, \mathbf{v}_s, \dot{\delta t}_s)$ and $(\mathbf{r}_r, \mathbf{v}_r, \dot{\delta t}_r)$ are the satellite and rover's 6D state and scalar clock drift, respectively. The geometric component is computed from the line-of-sight projection of the relative satellite-rover velocity, using the light-time-corrected satellite state (denoted by *) and the rover state at reception. Mathematical details of the first-order light-time correction used can be found in Coimbra and Gao (2026b). After modeling satellite ephemeris and clock errors separately, the measurement noise variance is dominated by thermal noise in carrier tracking (Kaplan & Hegarty, 2017). According to O'Dea et al. (2019), the downlink thermal noise contribution for one-way Doppler measurements is as follows.

$$\sigma^2_{\dot{\rho}} = \frac{2B_D}{C/N_0 \cdot S_L}\left(\frac{c}{2\pi f T_D}\right)^2 \quad , \tag{5}$$

where B_D is the bandwidth of the Doppler carrier loop, S_L is the squaring loss of the Costas loop, T_D is the integration time, and C/N_0 is in Hz.

In this study, we also investigate the improvement in rover localization by using the Doppler measurement from the satellite to the lander (l) with a weaker signal strength that is representative for a lander's antenna gain. The observed Doppler shift on the satellite-lander link is computed using the same model as in Equation 4, with the rover state replaced by the lander state $(\mathbf{r}_l, \mathbf{v}_l, \dot{\delta t}_l)$ and with the corresponding link-specific measurement noise. Note that the lander is stationary, so $\mathbf{v}_l = \mathbf{0}$.

2.3.2 | Pseudorange

The observed pseudorange $\tilde{\rho}$ between the lander and rover is defined as follows.

$$\tilde{\rho} = \|\mathbf{r}_l - \mathbf{r}_r\| + c\left(\delta t_r - \delta t_l\right) + \varepsilon_\rho \quad , \quad \varepsilon_\rho \sim \mathcal{N}\left(0, \sigma^2_\rho\right) \quad , \tag{6}$$

where δt represents the clock bias of each asset and ε_ρ is the pseudorange measurement noise with variance σ^2_ρ. Light-time delay is neglected for the rover-lander link because the corresponding propagation time is negligible over the distances considered.

As is done for the Doppler measurement noise, the pseudorange measurement noise is modeled using the thermal noise variance associated with an early-late delay lock loop (DLL) discriminator (Kaplan & Hegarty, 2017).

$$\sigma^2_\rho = \left(\frac{c}{R_c}\right)^2 \frac{B_r D}{2C/N_0}\left(1 + \frac{2}{T_r \cdot C/N_0(2-D)}\right) \tag{7}$$

The parameters for the chipping rate R_c, DLL bandwidth B_r, integration time T_r, and correlator spacing D are defined in Section 4. The chipping rate R_c is used to convert σ^2_ρ from chips^2 to m^2, when using C/N_0 in Hz.

2.3.3 | Differential Doppler Correction

When leveraging the additional Doppler measurement between the satellite and the lander, we assume that the lander relays its Doppler measurements to the rover over the surface link, allowing the rover to perform a differential Doppler correction to improve its state estimate.

$$\Delta\tilde{\dot{\rho}} = \tilde{\dot{\rho}}_r - \tilde{\dot{\rho}}_l \tag{8}$$

$$= (\mathbf{v}_s^* - \mathbf{v}_r) \cdot \frac{\mathbf{r}_s^* - \mathbf{r}_r}{\|\mathbf{r}_s^* - \mathbf{r}_r\|} + c\left(\dot{\delta t}_r - \dot{\delta t}_s\right) + \varepsilon_{\dot{\rho},r} - (\mathbf{v}_s^* - \mathbf{v}_l) \cdot \frac{\mathbf{r}_s^* - \mathbf{r}_l}{\|\mathbf{r}_s^* - \mathbf{r}_l\|} - c\left(\dot{\delta t}_l - \dot{\delta t}_s\right) - \varepsilon_{\dot{\rho},l} \tag{9}$$

$$= (\mathbf{v}_s^* - \mathbf{v}_r) \cdot \frac{\mathbf{r}_s^* - \mathbf{r}_r}{\|\mathbf{r}_s^* - \mathbf{r}_r\|} - (\mathbf{v}_s^* - \mathbf{v}_l) \cdot \frac{\mathbf{r}_s^* - \mathbf{r}_l}{\|\mathbf{r}_s^* - \mathbf{r}_l\|} + c\left(\dot{\delta t}_r - \dot{\delta t}_l\right) + \varepsilon_{\Delta\dot{\rho}} \tag{10}$$

$$\varepsilon_{\Delta\dot{\rho}} \sim \mathcal{N}\left(0, \sigma_{\dot{\rho},r}^2 + \sigma_{\dot{\rho},l}^2\right) \tag{11}$$

Since both Doppler shifts are received by the rover and lander at the same epoch, the satellite clock drift term cancels exactly, leaving the difference in geometric pseudorange rates, the relative rover-lander clock drift, and the measurement noise. Note that the variance of the difference of two independent random variables is the sum of their variances, so the thermal noise variances are added together in the differential Doppler measurement. The differential Doppler correction is measured only when both the rover and the lander see the satellite and when the rover-lander surface link is above the radio horizon.

3 | FILTERING AND OBSERVABILITY

This section discusses the filtering method used to process the measurements as well as the observability analysis used to interpret the measurement geometry. All filters presented in this study are variants of a single EKF that uses odometry as the process model and applies radiometric measurement updates. Odometry is used as the control input, and the mathematical details of the state and covariance propagation in the EKF's predict step are provided in Coimbra and Gao (2026b). This section describes only what is specific to the lander-aided architecture, including the state composition per measurement configuration, the Schmidt-Kalman approach for handling the ephemeris error, the prediction of differential Doppler measurements, and the observability analysis.

3.1 | Filter per Measurement Configuration

Each measurement configuration estimates the 3D rover position $\mathbf{r}_r$ as well as the clock and ephemeris states that the measurements in that configuration constrain. Rover velocity is not estimated as an independent state because the rover motion measured by odometry is used directly as the control input for state propagation and in the Doppler measurement prediction. Odometry uncertainty is incorporated into the corresponding noise models, leaving position $\mathbf{r}_r$ as the only kinematic state whose accumulated dead-reckoning error is corrected by the radiometric measurements. Table 1 lists the resulting state vectors that are estimated by the EKF for each measurement configuration. Every radiometric measurement is sensitive to a clock difference. For satellite-derived Doppler measurements, the state includes rover-satellite relative drift $c(\dot{\delta t}_r - \dot{\delta t}_s)$, and for lander-derived pseudorange measurements, the state includes the rover-lander relative bias $c(\delta t_r - \delta t_l)$ and drift $c(\dot{\delta t}_r - \dot{\delta t}_l)$. The rover-lander relative bias and drift follow the same two-state model as a single clock with summed diffusion coefficients because the rover and lander clocks are modeled as independent two-state stochastic processes. The broadcast ephemeris error is carried as a consider state $\boldsymbol{\delta}\mathbf{x}_{\text{eph}}$ only when the rover processes raw Doppler measurements. Section 3.2 elaborates on the formulation of the consider state within the filter. The differential correction does not use the consider state because the similar rover and lander LOS geometries to the satellite substantially reduce ephemeris error sensitivity through differencing, as explained in Section 3.3. Although the differential and lander-only configurations share the same 5D state, the differential configuration is better constrained because the differential Doppler measurement directly observes the relative rover-lander clock drift.

3.2 | Schmidt-Kalman Filter

When the rover processes raw Doppler measurements from the satellite, the broadcast ephemeris errors described in Section 2.1 perturb the observable through errors in the satellite position and velocity. In Coimbra and Gao (2026b), this effect was approximated in the filter using a scalar bias state with first-order Gauss-Markov dynamics. However, sensitivity tests with increased initial rover position uncertainty showed that a Schmidt-Kalman formulation using the Cartesian ephemeris-error state

TABLE 1
Filter state per measurement configuration.

Measurement	$\mathbf{r}_r$	$c(\dot{\delta t}_r - \dot{\delta t}_s)$	$c(\delta t_r - \delta t_l)$	$c(\dot{\delta t}_r - \dot{\delta t}_l)$	$\boldsymbol{\delta}\mathbf{x}_{\text{eph}}$	**Dimension**
Dimension	*3*	*1*	*1*	*1*	*9*	–
Odometry only	✓					3
Satellite (S)	✓	✓			✓	13
Lander (L)	✓		✓	✓		5
S + L	✓	✓	✓	✓	✓	15
Differential S + L	✓		✓	✓		5

yielded lower rover position error than an EKF that estimated the scalar bias. We therefore augment the filter with the ephemeris-error state $\boldsymbol{\delta}\mathbf{x}_{\text{eph}} = [\boldsymbol{\delta r}_s^\top, \boldsymbol{\delta v}_s^\top, \boldsymbol{\delta a}_s^\top]^\top \in \mathbb{R}^9$ and treat it as a consider state in a Schmidt-Kalman filter (Schmidt, 1966). A consider state represents an uncertain quantity whose covariance and cross-covariance with the estimated states are propagated, while its corresponding Kalman gain rows are set to zero so that it is not directly estimated. This allows its uncertainty to influence the estimated-state covariance without attempting to estimate a poorly observable state that could otherwise absorb measurement information and reduce improvement in the states of interest. In this case, the covariance of $\boldsymbol{\delta}\mathbf{x}_{\text{eph}}$ and its cross-covariance with the estimated states are propagated using the same Singer stochastic model described by Coimbra and Gao (2026b). During the measurement update, the cross-covariance allows the ephemeris uncertainty to affect the estimated state and its covariance. This treatment is appropriate because measurements from a single satellite do not provide sufficient information to estimate the full ephemeris error state.

The Doppler observable is sensitive to ephemeris errors because the filter forms the predicted measurement from the broadcast state $\tilde{\mathbf{r}}_s = \mathbf{r}_s + \boldsymbol{\delta r}_s$ and $\tilde{\mathbf{v}}_s = \mathbf{v}_s + \boldsymbol{\delta v}_s$. Since the EKF innovation is defined as observed minus the predicted measurement, the consider-state Jacobian $\mathbf{H}_c$ is therefore the negative of the predicted-measurement sensitivity to the broadcast ephemeris error. For the range-rate observable, which depends directly only on the relative satellite-rover position and velocity, the Jacobian reduces as follows.

$$\mathbf{H}_c = -\begin{bmatrix} \frac{\partial \hat{\dot{\rho}}}{\partial \boldsymbol{\delta r}_s} & \frac{\partial \hat{\dot{\rho}}}{\partial \boldsymbol{\delta v}_s} & \frac{\partial \hat{\dot{\rho}}}{\partial \boldsymbol{\delta a}_s} \end{bmatrix} = \begin{bmatrix} \frac{\partial \hat{\dot{\rho}}}{\partial \mathbf{r}_r} & -\mathbf{e}_r^\top & \mathbf{0}^\top \end{bmatrix} \quad , \tag{12}$$

where $\hat{\dot{\rho}}$ is the predicted pseudorange rate and $\mathbf{e}_r$ is the rover-satellite line-of-sight (LOS) unit vector.

To explicitly define the Schmidt-Kalman filter, let us partition the matrices into estimated (x) and consider (c) blocks as follows. Here, $\mathbf{x}_c := \boldsymbol{\delta}\mathbf{x}_{\text{eph}}$ and $\mathbf{x}_x$ contains all other states in Table 1 per measurement configuration.

$$\mathbf{x} = \begin{bmatrix} \mathbf{x}_x \\ \mathbf{x}_c \end{bmatrix} \quad , \quad \mathbf{P} = \begin{bmatrix} \mathbf{P}_{xx} & \mathbf{P}_{xc} \\ \mathbf{P}_{cx} & \mathbf{P}_{cc} \end{bmatrix} \quad , \quad \mathbf{H} = \begin{bmatrix} \mathbf{H}_x & \mathbf{H}_c \end{bmatrix} \quad , \quad \mathbf{K} = \begin{bmatrix} \mathbf{K}_x \\ \mathbf{K}_c \end{bmatrix} \tag{13}$$

The rover velocity is not a state and is instead taken from odometry, which makes the odometry process noise and measurement noise correlated. This correlation is handled by using a cross-correlated noise update, as described in Grewal and Andrews (2001). Coimbra and Gao (2026b) describe in detail the state and covariance update step in this modified EKF. In this work, the filter applies the same equations using the matrix partitioning in Equation 13 and forces the consider-block Kalman gain $\mathbf{K}_c = \mathbf{0}$. Thus, the Schmidt-Kalman filter considers the LOS-projected ephemeris uncertainty in its innovation, and also the cross-covariance $\mathbf{P}_{xc}$ tracks how much of the position estimate has been contaminated by the ephemeris error.

3.3 | Differential Doppler Measurement Prediction

The measurement models in Section 2 are evaluated at the estimated rover state and the light-time-corrected satellite state to form the predicted measurements and Jacobians. As mentioned in Section 2.3.3, the satellite clock drift cancels in the differential Doppler measurement. However, broadcast ephemeris error enters through the filter prediction because the predicted Doppler terms are evaluated using the same broadcast satellite state. To show this, let $\hat{\dot{\rho}} = f(\mathbf{x}_s)$ and $\boldsymbol{\delta}\mathbf{x}_{\text{eph}}^{rv} = [\boldsymbol{\delta r}_s^\top, \boldsymbol{\delta v}_s^\top]^\top \in \mathbb{R}^6$. If we

Taylor expand about the true satellite state $\mathbf{x}_s$, we find that a small ephemeris error produces a first-order prediction error in the pseudorange rate.

$$f(\mathbf{x}_s + \boldsymbol{\delta}\mathbf{x}^{rv}_{\text{eph}}) \simeq f(\mathbf{x}_s) + \frac{\partial f}{\partial \mathbf{x}_s}\boldsymbol{\delta}\mathbf{x}^{rv}_{\text{eph}} \tag{14}$$

$$\delta\hat{\dot{\rho}} \simeq \frac{\partial \hat{\dot{\rho}}}{\partial \mathbf{x}_s}\boldsymbol{\delta}\mathbf{x}^{rv}_{\text{eph}} \tag{15}$$

This prediction error motivates the inclusion of the consider block when using only raw satellite Doppler updates. For the differential Doppler configuration, the predicted differential measurement is

$$\Delta\hat{\dot{\rho}} = \hat{\dot{\rho}}_r(\tilde{\mathbf{x}}_s, \hat{\mathbf{x}}_r) - \hat{\dot{\rho}}_l(\tilde{\mathbf{x}}_s, \mathbf{x}_l) + \hat{d}_{rl} \quad , \tag{16}$$

where $d_{rl} := c(\dot{\delta t}_r - \dot{\delta t}_l)$ and $\hat{d}_{rl}$ represents the filter's estimate of d_{rl}. Both predicted Doppler terms use the same noisy broadcast satellite state $\tilde{\mathbf{x}}_s$. The corresponding ephemeris-induced prediction error is

$$\delta\left(\Delta\hat{\dot{\rho}}\right) \simeq \left(\frac{\partial \hat{\dot{\rho}}_r}{\partial \mathbf{x}_s} - \frac{\partial \hat{\dot{\rho}}_l}{\partial \mathbf{x}_s}\right)\boldsymbol{\delta}\mathbf{x}^{rv}_{\text{eph}} \tag{17}$$

Since the rover and lander are separated by only a few kilometers while the satellite range is thousands of kilometers, their LOS geometries to the satellite are nearly identical. We approximate the differential term in Equation 17 as zero, motivating the omission of the ephemeris consider state in the differential configuration. While the ephemeris error is not exactly removed from the physical measurement, its effect on the filter prediction is reduced by similar rover and lander LOS sensitivities.

3.4 | Observability

Due to the weak observability of the system, it is crucial to quantify which directions of rover position are well constrained by the available radiometric measurements. We perform this analysis using a noise-weighted linearized Fisher information matrix, which can be interpreted as a sum of measurement constraints over a fixed time window (Kay, 1993).

For time t, let $\mathcal{W}(t)$ denote the set of measurement epochs contained in a sliding one-hour window. For measurements with Jacobian $\mathbf{H}_k$ and measurement noise variance R_k (defined in Coimbra and Gao (2026b)), the accumulated Fisher information matrix $\mathbf{G}$ is as follows (Ober, 2002).

$$\mathbf{G} = \sum_{k\in\mathcal{W}(t)} \frac{1}{R_k}\mathbf{H}_k^\top \mathbf{H}_k + \mathbf{G}_0 \quad , \tag{18}$$

where $\mathbf{G}_0$ represents prior information on the estimated states. A weak position prior is included to regularize the matrix for the inversion in Equation 21 while having negligible influence along measurement-observed directions. The Jacobians are evaluated for a stationary rover so that the metric isolates the measurement geometry rather than a particular rover trajectory.

In this study, we focus primarily on estimating the rover 3D position $\mathbf{r}_r$. However, the measurements also depend on nuisance states, such as clock and ephemeris states. We therefore partition the information matrix into a rover-position block (r) and a nuisance-state block (n) as follows.

$$\mathbf{G} = \begin{bmatrix} \mathbf{G}_{rr} & \mathbf{G}_{rn} \\ \mathbf{G}_{nr} & \mathbf{G}_{nn} \end{bmatrix} \tag{19}$$

We want to determine how much position information remains after accounting for the fact that the nuisance states are also unknown. These nuisance states can explain part of the same measurement residuals as rover-position error, so using only the position block $\mathbf{G}_{rr}$ would overstate the available position information. We therefore compute the position-only information matrix using the Schur complement $\mathbf{G}_\mathbf{r}$ (Shen & Win, 2010).

$$\mathbf{G}_\mathbf{r} = \mathbf{G}_{rr} - \mathbf{G}_{rn}\mathbf{G}_{nn}^{-1}\mathbf{G}_{nr} \tag{20}$$

The Cramér-Rao lower bound (CRLB) gives a lower bound on the covariance of an unbiased estimator under the assumed measurement model. In this work, we use the CRLB as a geometric diagnostic. If a measurement provides little information in one direction, then the best possible estimator must have large uncertainty in that direction, or large CRLB. The CRLB is defined as the inverse of the Fisher information matrix, so the position CRLB covariance is the inverse of the Schur complement $\mathbf{G_r}^{-1}$. To quantify the uncertainty along a unit direction $\hat{\mathbf{u}}$, we project the position CRLB covariance onto that direction.

$$\sigma^2(\hat{\mathbf{u}}) = \hat{\mathbf{u}}^\top \mathbf{G_r}^{-1} \hat{\mathbf{u}} \tag{21}$$

In Section 5, we use σ as the observability metric, where it represents the standard deviation lower bound obtained by projecting the position CRLB covariance onto a unit direction. It represents the best-case 1σ position uncertainty along that direction under the assumed measurement and noise models in the one-hour window.

4 | SIMULATION SET-UP

This section summarizes the key simulation parameters used to model a realistic mission setting and validate the filter design. We first describe the initial states of the rover, satellite, and lander, along with their onboard clock parameters. We then specify the signal link assumptions and measurement noise parameters used for each observable. Finally, we describe the three mission scenarios used to evaluate performance and justify the filter design choices made in this study.

4.1 | Asset Initialization and Payloads

The satellite is in an elliptical lunar frozen orbit (ELFO) with orbital elements defined in Surrey Satellite Technology Ltd (2022). The resulting orbit has a period of 10.84 hours. Given that the lunar south pole is a region of high scientific interest, we initialize the rover's position to be at the Artemis Basecamp ($87.0°$ S, $50.5°$ E) (Keane et al., 2022). The lander's position uncertainty is set to be 5 m per-axis and is incorporated into the lander pseudorange measurement covariance by combining with the thermal measurement variance. Under nominal conditions, the rover's initial position error is set to the same uncertainty as the lander's position error. We expect that this initial error is achievable through long-term satellite-based measurements or through human-in-the-loop map matching. When the rover is deemed lost, the rover's initial position error is increased to 100 m per-axis. To compute the maximum surface separation between the rover and lander in Equation 3, we set the rover and lander antenna heights to be 1.5 m and 5.0 m, respectively.

In this study, the satellite and lander carry a Spectratime Rubidium Atomic Frequency Standard (RAFS) oscillator on board. We assume that the rover will be equipped with a cheaper and lighter clock, so we model a chip-scale atomic clock (CSAC) for the rover's oscillator. The diffusion coefficients for the RAFS and CSAC are disclosed in Coimbra and Gao (2026b).

4.2 | Signal Parameters

In Section 2, we define the carrier-to-noise density ratio C/N_0 in terms of the frequency f of the signal, maximum EIRP, and receiver gain. These parameters are listed in Table 2. The satellite transmitter parameters, including its boresight-to-half-power angle θ_{HP} at $7.1°$, are derived from Surrey Satellite Technology Ltd (2022). The rover's low- and high-gain antennas are based on the Endurance rover antenna (Keane et al., 2022). The high-gain antenna tracks the satellite, and the omnidirectional low-gain antenna is used to receive the lander measurements. The lander receiver and omnidirectional transmitter antennas are modeled after the parameters in ITU, Radiocommunication Sector (2025). The lander receiver is a fixed-beam, low-gain antenna that is not tracking the satellite, resulting in weaker signal strength than the satellite-rover link.

TABLE 2
Link parameters to compute the carrier-to-noise density ratio C/N_0. The receiver gain G_r includes a -0.5 dBi penalty to account for losses.

Parameter	Satellite-rover	Satellite-lander	Rover-lander
Frequency f [MHz]	2050	2050	2600
Maximum $EIRP_0$ [dBW]	26.5	26.5	-2
Receiver gain G_r [dBi]	22	2.5	-0.5

The measurement noise for Doppler and pseudorange is driven by the thermal noise in carrier tracking, as explained in Section 2.3. Table 3 outlines the relevant thermal noise parameters for both radiometric measurements (Giordano et al., 2023; Kaplan & Hegarty, 2017; O'Dea et al., 2019). The additional parameters needed to compute the Doppler measurement noise, such as the squaring loss of the Costas loop, are included in Coimbra and Gao (2025).

TABLE 3
Thermal noise parameters for Doppler and pseudorange measurements.

Parameter	Value
Doppler bandwidth B_D	1 Hz
Integration time T_D	0.02 seconds
Chipping rate R_c	1.023 Mcps
DLL bandwidth B_r	1 Hz
DLL correlator spacing D	0.5 chips
Integration time T_r	0.02 seconds

For the signal to be received, we apply a 30 dB-Hz threshold to the carrier-to-noise density ratio C/N_0. However, no geometrically visible link falls below the threshold since the satellite elevation mask at $5°$ proves to be the limiting factor for signal availability, as seen in Figure 2.

4.3 | Mission Scenarios

In this study, we investigate three mission scenarios: (A) the rover travels in a circle around the lander, maintaining constant LOS at a distance of 1.91 km away; (B) the rover is deployed from the lander with a 5 m per-axis initial position error and drives away in a continuous straight line and eventually goes beyond LOS; (C) the rover is lost with a 100 m per-axis initial position error and drives in a continuous straight line, eventually passing within the lander radio horizon before losing LOS with the lander again. Using the maximum surface separation formulation in Equation 3, the lander radio horizon is computed to be 6.45 km. The motion profiles for the missions are shown in Figure 2.

For all missions, the simulation window is exactly 24 hours and the rover speed is 0.5 km/h, motivating the distances that the rover traverses in each mission. The rover speed is obtained from the average traverse speed of the Endurance rover (Keane et al., 2022). Doppler measurements and odometry are sampled at 1 Hz, whereas the lander-based measurements (pseudorange and differential Doppler) are sampled at 0.1 Hz. ODTS updates occur every 6 hours. The parameters for the broadcast ephemeris errors are justified and tabulated in Coimbra and Gao (2026b). The results in Section 5 are evaluated over 100 Monte Carlo realizations.

5 | RESULTS

This section evaluates how the proposed lander-aided architecture performs from both geometric and mission-level perspectives. We first use the projected position CRLB to compare the directions constrained by satellite Doppler, lander pseudorange, and their combination. We then isolate the effect of each measurement source using Mission A, where the rover remains within the lander radio horizon for the full simulation. Finally, we evaluate the filter performance under Missions B and C scenarios, where the lander link is lost or reacquired during the traverse, to assess whether the filter can preserve useful localization accuracy as the available measurement set changes.

5.1 | Observability

We investigate the observability of the satellite-only, lander-only, and satellite-and-lander measurement configurations. As defined in Section 3, the metric used is the standard deviation lower bound σ obtained by projecting the position CRLB covariance onto

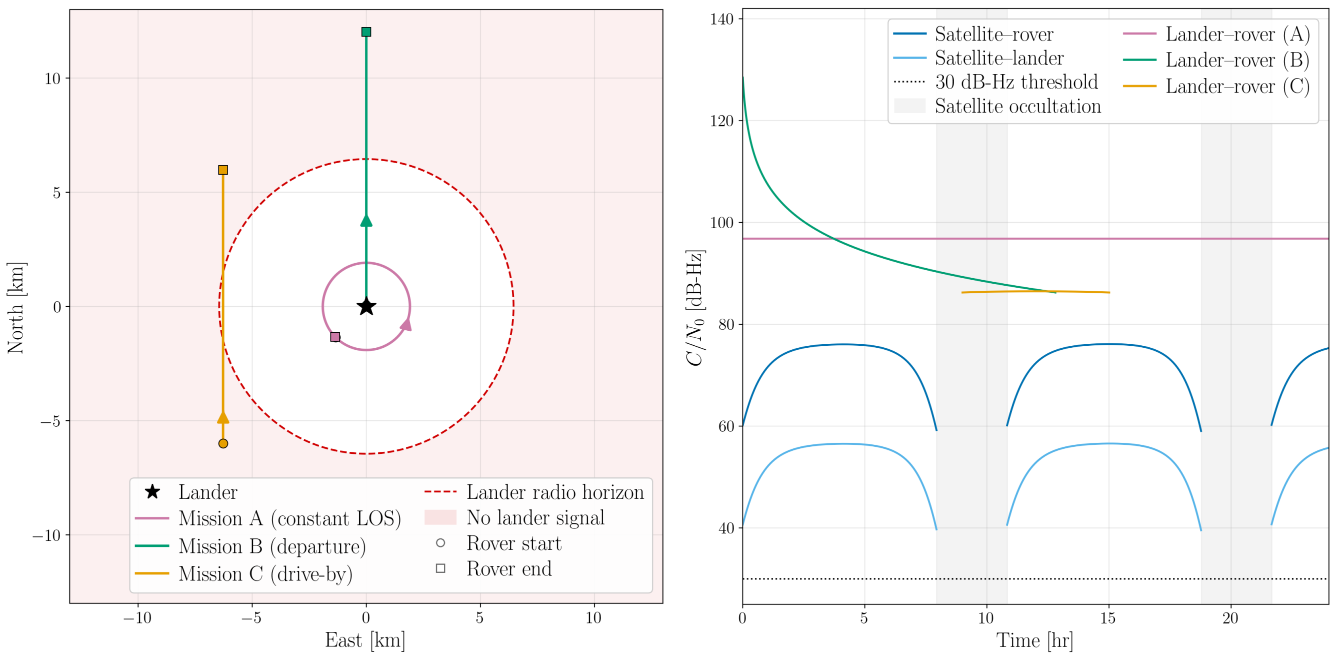

FIGURE 2 [Left] Top-down view of the motion profile for each mission scenario. [Right] Carrier-to-noise density ratio C/N_0 over time.

a specific unit direction. In Figure 3, we evaluate three directions, NE-SW, NW-SE, and Up, because the satellite sky track primarily sweeps across the NW-SE direction. For this analysis, the lander is placed at a favorable bearing (45° with respect to the rover) to evaluate the best-case improvement provided by the lander geometry. The lander-rover geometry is equivalent to the starting position of Mission A, but this analysis is performed for a stationary rover.

The σ vs. time curves are computed over sliding one-hour windows, so the plotted values begin one hour into the simulation and extend one hour into an occultation interval. For each measurement configuration, we also select a representative one-hour window from hours 14 to 15, and show the corresponding East-North 1σ ellipse. Small σ values indicate directions that are strongly constrained by the available measurements, while large values indicate weakly observable directions. In the satellite-only case, the NW-SE direction is generally the most observable because it aligns with the dominant direction of the satellite's apparent sky motion. In the selected one-hour window, the East-North ellipse shows that this direction is constrained to approximately 28 m, while the orthogonal NE-SW direction remains weakly constrained at approximately 2.5 km. In the lander-only case, the NE-SW direction is constrained because it is aligned with the rover-lander LOS. The orthogonal horizontal direction and the Up direction are weakly observable by comparison, since a single lander pseudorange measurement provides little information outside the LOS direction.

The satellite-and-lander configuration provides the strongest overall observability, as expected. The lander maintains a stable constraint in the NE-SW direction, giving an approximately 10 m lower bound throughout the simulation, while the satellite-based Doppler measurements improve the remaining directions relative to the satellite-only case. The NW-SE and Up directions exhibit two peaks per orbital pass. These peaks occur when the Doppler sensitivity in those directions varies weakly over the one-hour window, making the corresponding position error difficult to separate from the nuisance states. Although these peaks reflect a limitation of the windowed observability metric, the analysis still demonstrates the complementary benefits of the satellite and lander measurements. Lander ranging removes the kilometer-scale weak direction present in satellite-only Doppler, while satellite Doppler provides the time-varying geometry needed to constrain directions that lander ranging alone cannot resolve. We omit the differential measurement configuration from the observability analysis because it provides similar geometric constraints to the satellite-and-lander case.

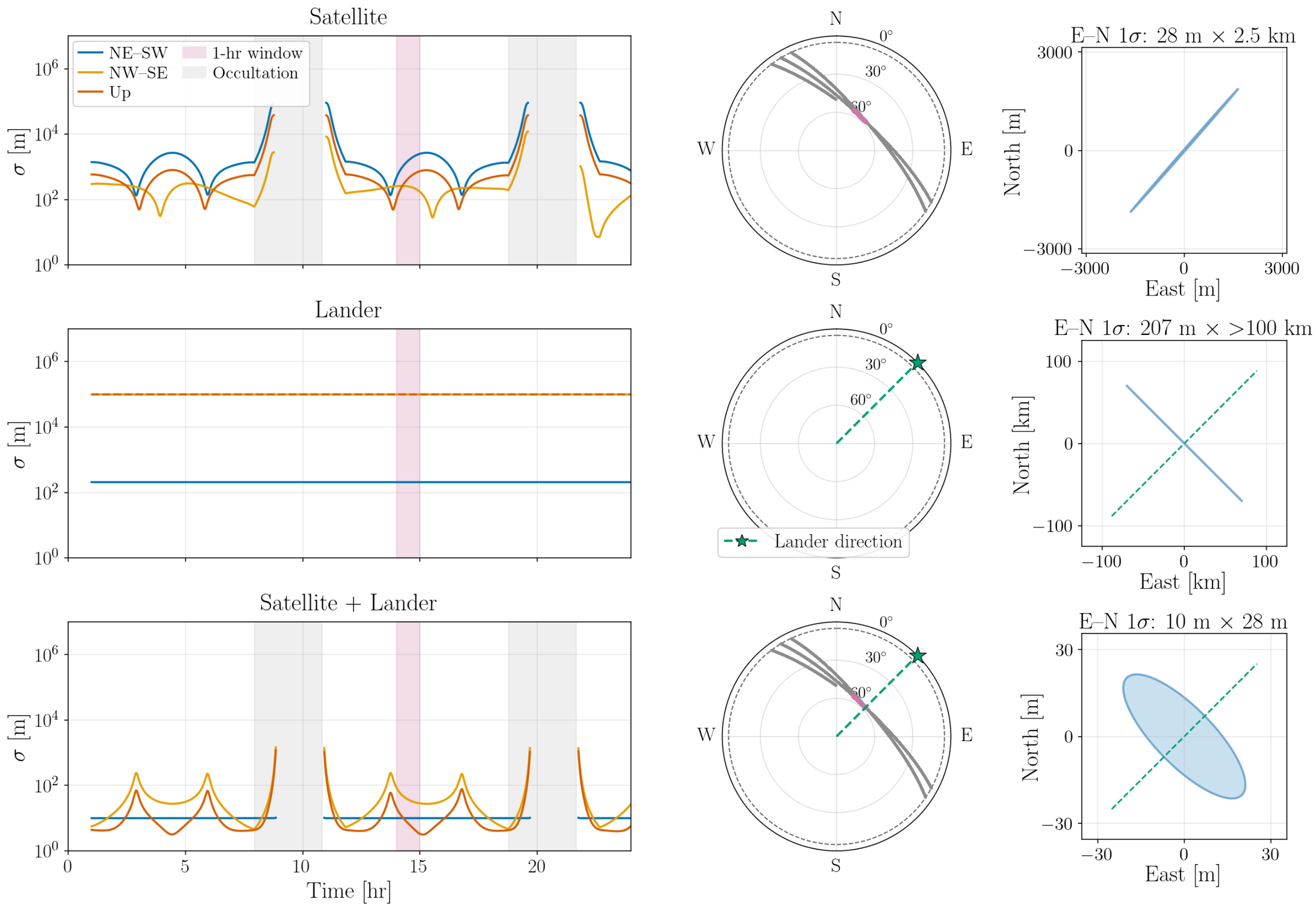

FIGURE 3 [Left column] The standard deviation lower bound σ obtained by projecting the position CRLB covariance $\mathbf{G_r}^{-1}$ onto one of three directions: NE-SW, NW-SE, and Up. The σ values for three measurement configurations are shown. [Middle column] Sky plot of the satellite and the direction of the lander with respect to the rover at center. The satellite's path during the selected 1-hour window is highlighted in pink. [Right column] East-North (E-N) 1σ ellipse for each measurement configuration at the selected 1-hour window. The title denotes the length of the major and minor axes of the ellipse.

5.2 | Ablation on Measurement Configurations

We compare the measurement configurations using Mission A for two primary reasons. First, the lander remains in constant LOS to the rover, ensuring that differences in performance are attributable to the measurement configuration rather than intermittent link availability. Second, the rover completes a full loop around the lander, reducing sensitivity to any single rover-lander-satellite geometry and making the comparison less dependent on a particularly favorable or unfavorable lander direction relative to the satellite ground track. For the ablation study, we initialize the rover with a 100 m position error along each axis to highlight the reduction in position error provided by each measurement configuration, as seen in Figure 4.

The odometry-only case does not have any external measurement source, so it cannot reduce the position error more than its initial position error. The lander case improves over the odometry-only case by 20 to 45 m. The satellite case outperforms the lander case, but has more fluctuations over time. We see a drastic improvement when using both Doppler and pseudorange measurements from the satellite and lander, respectively. The improvements due to ODTS updates are also more apparent in the satellite-and-lander case. Finally, the differential measurement configuration outperforms all other measurement configurations, reducing the position error to sub-10-m accuracy at 1.8 hours and maintaining that accuracy for the rest of the simulation. Figure 5 provides a more detailed view of how each measurement configuration affects localization performance by decomposing the position error into its ENU components.

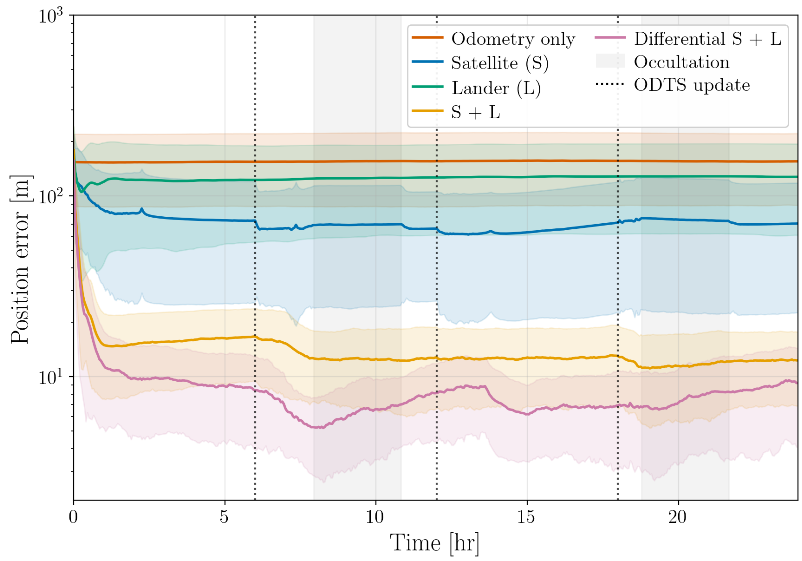

FIGURE 4 The rover's 3D position error norm over time for Mission A for each measurement configuration specified in Table 1. The mean position error across the Monte Carlo runs is shown in the solid line and the 1σ range is denoted by the shaded region.

The satellite case eventually reduces its 3D position error over time, whereas the lander case immediately reduces its position error in the north and east directions. However, the lander case is unable to reduce the error in the up direction, contributing to most of its 3D error norm in Figure 4. The satellite-and-lander case performs similarly to the lander case, except the satellite

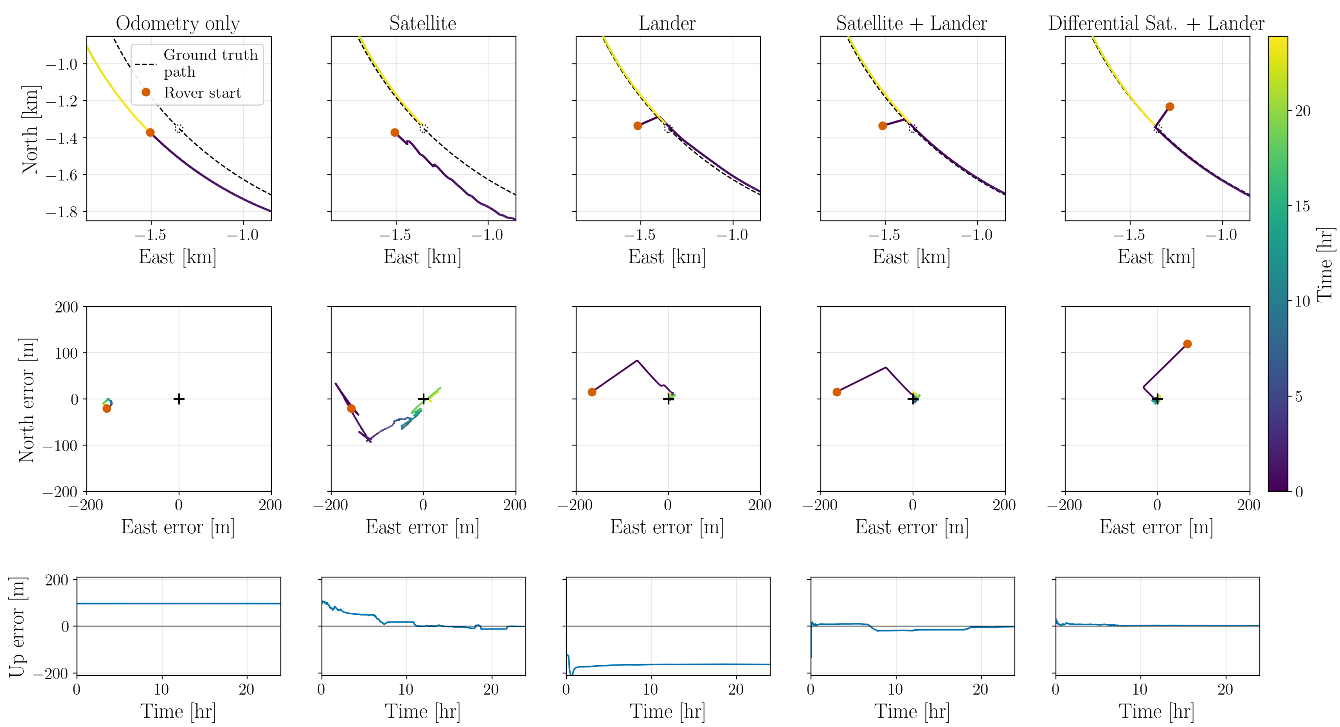

FIGURE 5 [Top row] Top-down view of the rover's ground-truth and estimated path per measurement configuration, zoomed into the start and end sections of the trajectory. [Middle row] North error vs. east error where the center corresponds to the rover's true position over time. [Bottom row] Up error over time. Note that these results correspond to a single Monte Carlo run.

assists in reducing the error in the up direction as well. Finally, we find that the differential case is able to reduce the position error in all three axes the most effectively.

5.3 | Localization Performance for Mission Scenarios

After evaluating the scenario where the lander is in continuous LOS, we stress-test the estimator in a scenario where the rover drives beyond the lander radio horizon. While the lander is visible, the filter uses the most informative configuration, consisting of differential rover-lander Doppler and rover-lander pseudorange. Once the rover-lander surface link drops below the horizon, differential Doppler and pseudorange are no longer available, so the filter switches to undifferenced satellite Doppler. Since the ephemeris error reduction is then lost, the satellite ephemeris consider state is reinstated, as shown in Table 1. States shared by both configurations retain their posterior mean and covariance, while newly introduced states are initialized from their prior distributions. The relative clock-drift state is mapped from the rover-lander drift to the rover-satellite drift by retaining the estimated rover-clock contribution and injecting the uncertainty associated with the unobserved lander-satellite drift difference. This avoids discarding rover clock information accumulated when the lander was visible, while preventing the switched filter from becoming overconfident.

Figure 6 shows the 3D rover position error for Mission B, in which the rover departs from the lander with good initial position knowledge and crosses the lander radio horizon at approximately 13 hours. After lander LOS is lost, the position error grows at a rate similar to the odometry-only case, indicating that undifferenced satellite Doppler provides limited benefit while the broadcast ephemeris error remains large. However, after the 18-hour ODTS update, the Doppler-based filter is able to reduce the position error relative to the odometry-only case. This behavior shows that satellite Doppler can still provide useful corrections after lander loss, but its benefit depends strongly on the quality of the broadcast ephemeris.

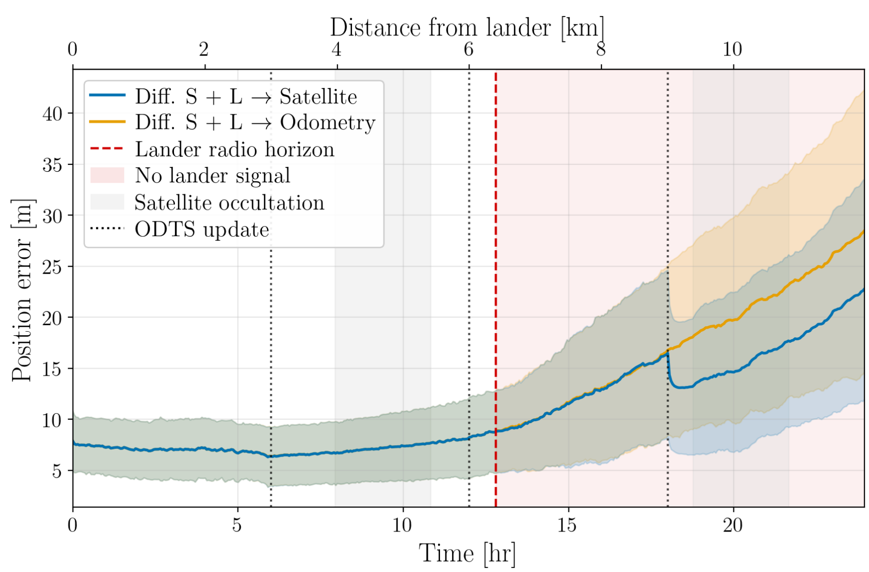

FIGURE 6 Position error over time for Mission B, where the rover departs from the lander and eventually loses lander LOS. The filter uses differential Doppler and rover-lander pseudorange while the lander link is available. After the rover crosses the lander radio horizon, the filter switches either to undifferenced satellite Doppler or to odometry-only propagation as a baseline.

Figure 7 shows the position error over time for Mission C, in which the rover is initially outside lander LOS, later regains the lander link, and then loses it again. When the lander is not visible, the filter uses undifferenced satellite Doppler. When the lander is visible, the filter switches to the differential satellite-and-lander configuration. Before the lander link is acquired, the satellite Doppler configuration gradually reduces the position error, with additional improvements following ODTS updates. Once the lander becomes visible at approximately 9 hours, the differential configuration produces a rapid reduction of the 1σ uncertainty band and a 60 m drop in the mean position error. During the lander-visible interval, the position error remains below 20 m. After the rover loses lander LOS again near 15 hours, the satellite Doppler configuration approximately maintains the achieved position accuracy, although the 1σ band grows relative to the lander-visible interval.

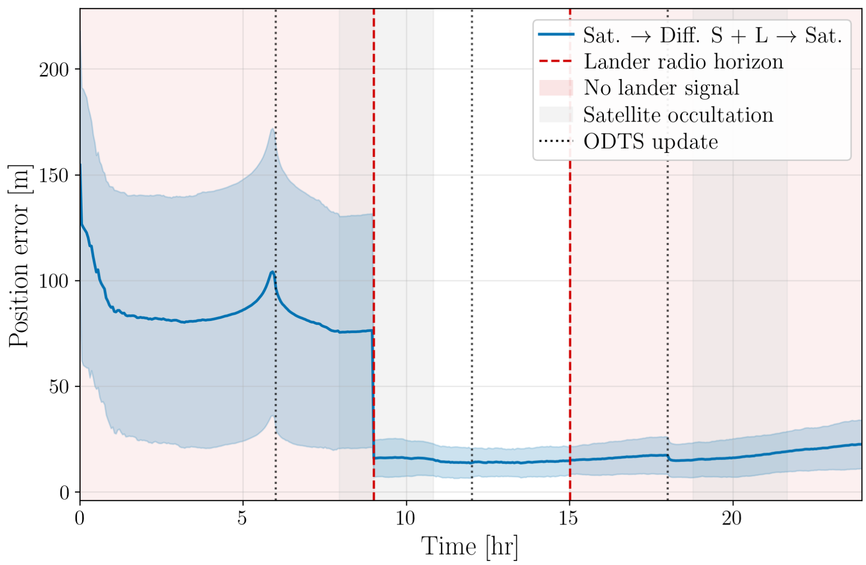

FIGURE 7 Position error over time for Mission C, where the rover is initially lost, enters the lander radio horizon region, and then exits it again. The filter uses the differential satellite-and-lander configuration when lander measurements are available and undifferenced satellite Doppler otherwise.

6 | CONCLUSION

This paper evaluated a lander-aided navigation architecture for lunar rovers operating with minimal infrastructure. The rover uses one-way Doppler from a single relay satellite, one-way pseudorange from a known surface lander, and onboard odometry. We formulated EKF variants for each measurement configuration and used a Schmidt-Kalman consider-state treatment to account for broadcast ephemeris uncertainty when raw satellite Doppler is processed. We also introduced a differential Doppler configuration in which the lander forwards its satellite Doppler observation to the rover, reducing sensitivity to common satellite clock and ephemeris errors.

The observability analysis showed that satellite Doppler and lander pseudorange can provide highly complementary constraints when the rover-lander LOS is orthogonal to the satellite sky-track sweep. Using both satellite Doppler and lander ranging strongly constrains the rover-lander LOS direction relative to the satellite-only case and improves vertical observability relative to the lander-only case. When the rover is in constant LOS with the lander, the differential satellite-and-lander configuration achieves the best performance relative to all other measurement configurations. For the mission case study when the rover travels beyond lander LOS, the estimator maintains useful accuracy when switching from a differential measurement configuration to a Doppler-only configuration and the Doppler measurements prove useful over odometry-only propagation following ODTS updates. We also evaluated a scenario where the rover is initially lost at 100 m per-axis position error and reacquires the lander link. At the time of lander signal reacquisition, the mean position error is reduced by approximately 60 m, and the rover maintains an accuracy of approximately 20 m even after losing the signal again.

These results suggest that a lander can serve as a valuable navigation reference for early lunar rover missions before dense lunar PNT infrastructure is available. Furthermore, the geometry and mission case studies presented in this work can help inform operational concepts for near-term missions. Future work will incorporate terrain-aware visibility, near-horizon propagation effects, and sensitivity analyses on the assets' oscillator assumptions.

ACKNOWLEDGMENTS

This research is supported by the Stanford Knight-Hennessy Scholars fellowship and the National Science Foundation (NSF) Graduate Research Fellowship No. DGE-2146755. We would like to thank the other members of the Stanford Navigation and Autonomous Vehicles Laboratory for their helpful discussions and support. We also acknowledge the Blue Origin team for communications and for providing information on mission scenario assumptions.

REFERENCES

Cauligi, A., Swan, R. M., Ono, H., Daftry, S., Elliott, J., Matthies, L., & Atha, D. (2023). ShadowNav: Crater-based localization for nighttime and permanently shadowed region lunar navigation. *2023 IEEE Aerospace Conference*, 1–12. https://doi.org/10.1109/AERO55745.2023.10115745

Coimbra, K. M. Y., Cortinovis, M., Mina, T., & Gao, G. (2025). Single-satellite lunar navigation via Doppler shift observables for the NASA Endurance mission. *NAVIGATION: Journal of the Institute of Navigation*, *72*(3). https://doi.org/10.33012/navi.710

Coimbra, K. M. Y., & Gao, G. (2025). Comparative Analysis and Design of a Dual-Satellite System for Lunar Rover Localization. *2025 IEEE Aerospace Conference*, 1–11. https://doi.org/10.1109/AERO63441.2025.11068589

Coimbra, K. M. Y., & Gao, G. (2026a). Lander-Aided Differential Doppler and One-Way Ranging for Lunar Rover Navigation with a Single Relay Satellite [Abstract accepted]. *Proceedings of the 39th International Technical Meeting of the Satellite Division of The Institute of Navigation (ION GNSS+ 2026)*.

Coimbra, K. M. Y., & Gao, G. (2026b). Time-Correlated Ephemeris Errors and Relativistic Effects for Single-Satellite Doppler Localization of Lunar Rovers [Abstract accepted]. *Proceedings of the 39th International Technical Meeting of the Satellite Division of The Institute of Navigation (ION GNSS+ 2026)*.

Daftry, S., Chen, Z., Cheng, Y., Tepsuporn, S., Khattak, S., Matthies, L., Coltin, B., Naal, U., Ma, L. M., & Deans, M. (2023). LunarNav: Crater-based localization for long-range autonomous lunar rover navigation. *2023 IEEE Aerospace Conference*, 1–15. https://doi.org/10.1109/AERO55745.2023.10115640

Dai, A., Wu, A., Iiyama, K., Casadesus Vila, G., Coimbra, K. M. Y., Deng, T., & Gao, G. (2025). Full Stack Navigation, Mapping, and Planning for the Lunar Autonomy Challenge. *Proceedings of the 38th International Technical Meeting of the Satellite Division of The Institute of Navigation (ION GNSS+ 2025)*, 1986–2002. https://doi.org/10.33012/2025.20447

Delépaut, A., Giordano, P., Ventura-Traveset, J., Blonski, D., Schönfeldt, M., Schoonejans, P., Aziz, S., & Walker, R. (2020). Use of GNSS for lunar missions and plans for lunar in-orbit development. *Advances in Space Research*, *66*(12), 2739–2756. https://doi.org/10.1016/j.asr.2020.05.018

Giordano, P., Swinden, R., Gramling, C., Crenshaw, J., & Ventura-Traveset, J. (2023). LunaNet Position, Navigation, and Timing Services and Signals, Enabling the Future of Lunar Exploration. *Proceedings of the 36th International Technical Meeting of the Satellite Division of The Institute of Navigation (ION GNSS+ 2023)*, 3577–3588. https://doi.org/10.33012/2023.19345

Grewal, M. S., & Andrews, A. P. (2001). *Kalman Filtering: Theory and Practice Using MATLAB* (2nd) [ISBN: 9781118851210]. John Wiley & Sons.

International Astronomical Union. (2024). Resolution II: to establish a standard Lunar Celestial Reference System (LCRS) and Lunar Coordinate Time (TCL) [Official IAU resolution].

ITU, Radiocommunication Sector. (2025, March). *Technical and operational characteristics for space research systems in the vicinity of the Moon* (Report ITU-R No. SA.2553-0) (SA Series: Space applications and meteorology). International Telecommunication Union (ITU). Geneva, Switzerland.

Jun, W. W., Cheung, K.-M., & Lightsey, E. G. (2024). Real-time position, velocity, and timing estimation of lunar surface users with joint Doppler and ranging. *IEEE Transactions on Aerospace and Electronic Systems*, *60*(4), 5525–5537. https://doi.org/10.1109/TAES.2024.3396118

Kaplan, E. D., & Hegarty, C. (2017). *Understanding GPS/GNSS: Principles and applications* [ISBN: 9781630814427]. Artech House.

Kay, S. M. (1993). *Fundamentals of Statistical Signal Processing: Estimation Theory* [ISBN: 0133457117]. Prentice Hall.

Keane, J. T., Tikoo, S. M., & Elliot, J. (2022). Endurance: Lunar South Pole-Aitken basin traverse and sample return rover. *NASA Jet Propulsion Laboratory, Technical Report*. https://tinyurl.com/2p88fx4f.

Misra, P., & Enge, P. (2012). *Global Positioning System: Signals, Measurements & Performance* [ISBN-13: 978-0970954428]. Ganga-Jamuna Press.

Ober, R. J. (2002). The Fisher information matrix for linear systems. *Systems & Control Letters*, *47*(3), 221–226. https://doi.org/10.1016/S0167-6911(02)00190-1

O'Dea, A., Kinman, P., Pham, T. T., & Chang, C. (2019). Doppler tracking [DSN No. 810-005, 202, Rev. C]. *Deep Space Network*. https://deepspace.jpl.nasa.gov/dsndocs/810-005/202/202C.pdf.

Schmidt, S. F. (1966). Application of state-space methods to navigation problems. In *Advances in control systems* (pp. 293–340, Vol. 3). Elsevier. https://doi.org/10.1016/B978-1-4831-6716-9.50011-4

Shen, Y., & Win, M. Z. (2010). Fundamental limits of wideband localization—Part I: A general framework. *IEEE Transactions on Information Theory*, *56*(10), 4956–4980. https://doi.org/10.1109/TIT.2010.2060110

Singer, R. A. (1970). Estimating optimal tracking filter performance for manned maneuvering targets. *IEEE Transactions on Aerospace and Electronic Systems*, (4), 473–483. https://doi.org/10.1109/TAES.1970.310128

Surrey Satellite Technology Ltd. (2022). Lunar Pathfinder: Data relay satellite in orbit around the Moon [Service Guide (V4)]. *SSTL*. https://www.sstl.co.uk/getmedia/9efe3cc5-6b5b-4fd1-bbd7-443bc2d21848/Lunar-Pathfinder-Service-Guide-V004.pdf.

Tanaka, T., Jun, W. W., Ogbe, D., Kobayashi, M. M., & Cheung, K.-M. (2025). Lunar Positioning and Time Transfer via Single-Satellite Differential Dual One-Way Ranging. *IEEE Transactions on Aerospace and Electronic Systems*, *62*, 2980–2992. https://doi.org/10.1109/TAES.2025.3644278

Thompson, S., Martin, S., & Bevly, D. (2021). Single differenced Doppler positioning with low Earth orbit signals of opportunity and angle of arrival estimation. *Proceedings of the 2021 International Technical Meeting of the Institute of Navigation*, 497–509. https://doi.org/10.33012/2021.17845

Watson-Morgan, L. (2023, July). Human Landing System [NTRS Document ID: 20230010065].

Zhao, L., Lei, M., Liu, Y., Wang, Y., Ge, J., Guo, X., & Fang, Z. (2025). LEO-SOP differential Doppler/INS tight integration method under weak observability. *Electronics*, *14*(2), 250. https://doi.org/10.3390/electronics14020250